Green Chemistry

ROYAL SOCIETY OF CHEMISTRY

COMMUNICATION

View Article Online
View Journal | View Issue

Cite this: *Green Chem.*, 2023, **25**, 5404

Received 30th April 2023,
Accepted 20th June 2023

DOI: 10.1039/d3gc01420g

rsc.li/greenchem

High efficiency coupled electrocatalytic CO_2 reduction to C_2H_4 with 5-hydroxymethylfurfural oxidation over Cu-based nanoflower electrocatalysts†

Zonghang Zhang,[a] Shan Liu,[a] Zhao Wu,*[b] Xiaoyan Chen,[a] Jingui Wang,[a] Yuji Gao,[a] Shuai Wang,[a] Furong Tao[a] and Guangqiang Lv*[a]

To improve the total value of the redox products and energy conversion efficiency in CO_2 electroreduction (CO_2RR) and 5-hydroxymethylfurfural electrooxidation (HMFOR), commercial Cu foam was chemically oxidized into nanoflower CuO on its surface and used as an electrocatalyst in both CO_2RR and HMFOR. In CO_2RR, the prepared CuO nanoflower on Cu foam (CuO-NF@Cu) was quickly reduced to hybrid Cu_2O/Cu nanoflower (Cu_2O/Cu-NF@Cu). At a reduction potential of −0.95 V (*vs.* RHE), a high C_2H_4 faradaic efficiency (FE) up to 70% with a current density of 104.5 mA cm^{-2} can be obtained within 45 h of testing. In HMFOR, CuO-NF@Cu gave a 99.3% FDCA FE at a potential of 1.62 V (*vs.* RHE). Moreover, CO_2RR and HMFOR can be coupled together with CuO-NF@Cu as the anode electrocatalyst and Cu_2O/Cu-NF@GDL as the cathode electrocatalyst. A current density up to 188.8 mA cm^{-2} at a cell voltage of 2.75 V can be obtained. FEs of FDCA and C_2H_4 up to 96.6%/74.5%, respectively, were achieved in coupled CO_2RR-HMFOR within 5 h. This work makes it easy to simultaneously efficiently convert CO_2 to high-value C_2H_4 and upgrade a renewable biomass platform compound.

Introduction

The rapid development of industry over the past hundred years has led to the large-scale use of nonrenewable fossil resources, causing a substantial increase in the CO_2 concentration in the atmosphere.[1–4] Developing and utilizing renewable energy and resources, such as solar, wind, electric, and biomass resources, and selectively reducing CO_2 generated by fossil resources to valuable fuels or chemicals with clean and renewable energy is significant for future development.[5–7] The selective reduction of CO_2 (CO_2RR) into one specific multi-carbon product with high Faraday efficiency (FE) over one easily prepared electrocatalyst is far from practical application owing to the uncertain and kinetically sluggish C–C coupling and H addition.[8–12] Moreover, a sluggish oxygen evolution reaction (OER) at the anode results in high anodic potential and as high as 94.5% of the input energy is consumed at the anode with low-value O_2 produced.[13–15] Thus, substituting OER with reactions of lower energy requirements and value-added oxidative products would significantly reduce the anodic potentials, as well as raise the efficiency for CO_2RR.[16–18]

5-Hydroxymethylfurfural (HMF) is an important biomass-derived platform molecule. It can be oxidized into 2,5-furandicarboxylic acid (FDCA) under certain conditions.[19] FDCA has a similar molecular structure to terephthalic acid and can be used as an alternative chemical in the fields of fine chemicals and medicines.[20] Traditionally, the production of FDCA from HMF needs harsh reaction conditions, such as a high reaction temperature, high oxygen pressure and noble metal catalysts.[21,22] Electrocatalysis of HMF (HMFOR) can be conducted under mild conditions without high reaction temperature, high oxygen pressure, or an expensive catalyst.[23] However, the reported electrocatalysts for HMF oxidation are prepared with complicated procedures or give low FDCA selectivity.[24–26] On the other hand, the kinetics of the synergistic hydrogen evolution reaction (HER) at the cathode is not ideal and restricts the anode HMF oxidation. Thus, coupling CO_2RR and HMFOR seems an attractive approach to solving the above problem in CO_2RR and HMFOR. In this field, researchers have tried coupling CO_2RR (to formic acid, or CO) with HMFOR (to FDCA, maleic acid, formic acid),[18,27,28] CO_2RR (to CO or formate) with CH_3OH oxidation (to formate),[5,29] HMFOR (to FDCA) with 4-nitrophenol hydrogenation,[30] *etc.* Generally, only a C_1 product was achieved in the CO_2RR coupled reaction and there was low FDCA selectivity in the HMFOR coupled reaction with low current density and complicated, different electrocatalyst preparation procedures in the anode and cathode.[31] Therefore, an

[a]*Shandong Provincial Key Laboratory of Molecular Engineering, Qilu University of Technology (Shandong Academy of Sciences), Jinan 250353, Shandong, China. E-mail: lvguangqiang@qlu.edu.cn*
[b]*Safety and environmental protection department of Sinopec Jinan Company, Jinan, Shandong 250101, China. E-mail: wuzhao.jnlh@sinopec.com*

† Electronic supplementary information (ESI) available. See DOI: https://doi.org/10.1039/d3gc01420g

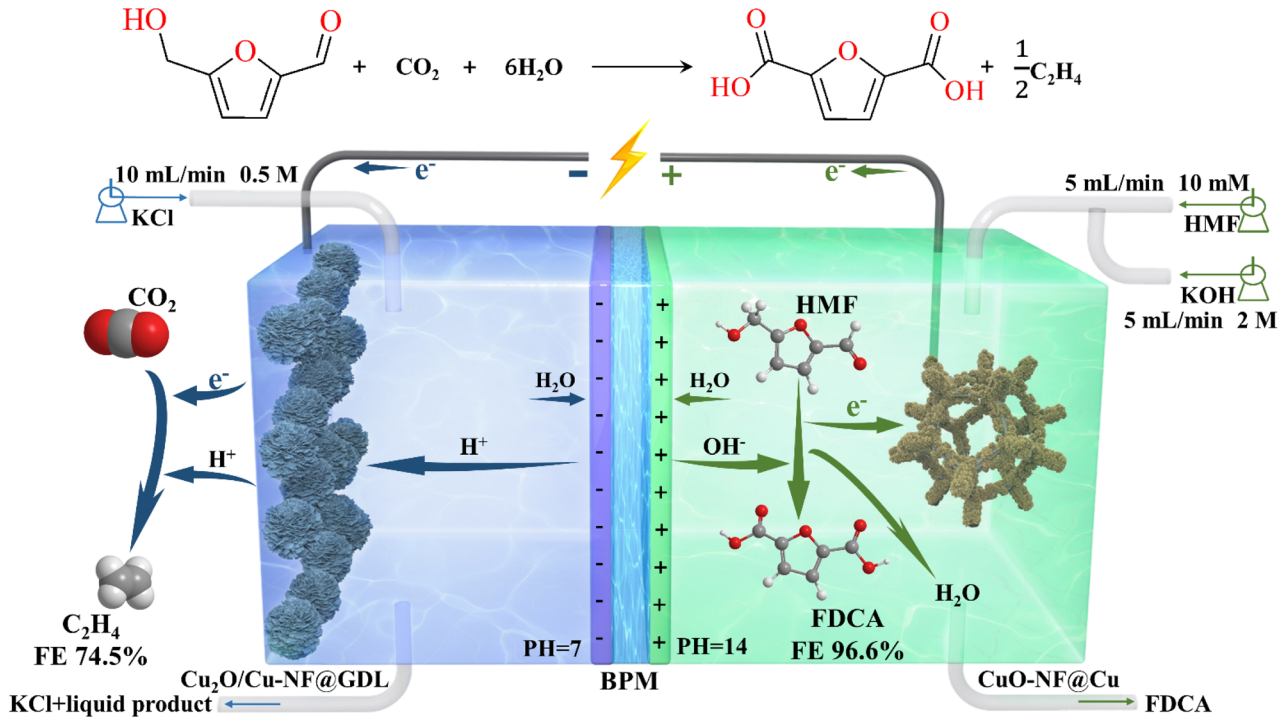

Fig. 1 Schematic illustration of integrated electrolysis flow cell coupling CO_2RR with HMFOR.

easily prepared electrocatalyst that can simultaneously give high FDCA selectivity in anode HMF oxidation and high FE in cathode CO_2RR to produce high-value C_2 products is very important for the utilization of renewable biomass resources, renewable electric energy, and cyclic utilization of CO_2 resources.

In the past decades, Au, Pt, Pd, Ru or their alloys have been widely studied as anode electrocatalysts in HMFOR.[32–34] Recently, studies on transition metal (Fe, Co, Ni, Cu, *etc.*) – based electrocatalysts have caused rapid development in HMFOR and even higher target product selectivity and energy efficiency have been obtained.[35–39] In general, researchers concluded that the active phases in HMF electrooxidation with transition metal catalysts should be their nitride or oxide compounds with unique nanostructures. The atomic vacancies and local structural disorder created by exotic species like oxygen,[37,40] nitride,[38] sulphur,[39,41] phosphorus,[36] and selenium,[42] the morphology of the nanostructure, and the valence states of the metal sites are responsible for their activity in HMFOR. In CO_2RR, a copper-based catalyst was shown to be an efficient electrocatalyst toward C_{2+} products.[43–46] Defect sites with low-coordinated Cu atoms and polarized $Cu^{\delta+}$ ($0 < \delta \leq 1$) were deemed responsible for promoting the C–C coupling step at low overpotentials in CO_2RR.[44] This feature indicates that one elaborately prepared oxide-derived Cu catalyst may be suitable in both CO_2RR and HMFOR as follows.

$$HMF + 6OH^- \rightarrow FDCA + 4H_2O + 6e^- \text{(Anode reaction)}$$

$$2CO_2 + 12H^+ + 12e^- \rightarrow C_2H_4 + 4H_2O \text{ (Cathode reaction)}$$

$$2CO_2 + 2HMF + 12H_2O \rightarrow C_2H_4 + 2FDCA \text{ (Overall reaction)}$$

Here, a simply prepared CuO nanoflower (CuO-NF) sheet over a Cu foam surface (CuO-NF@Cu) was prepared and used as the electrocatalyst in CO_2RR and HMFOR. In CO_2RR, the CuO-NF in the resultant CuO-NF@Cu quickly converted into the Cu_2O phase in CO_2RR and formed a stable Cu^+/Cu interface. The obtained Cu_2O/Cu-NF@Cu exhibited facilitated kinetics of CO_2RR into C_2H_4, leading to a high C_2H_4 FE of *ca.* 70% at −0.95 V (*vs.* RHE), along with a current density of 104.5 mA cm^{-2} within the tested 45 h. On the other side, CuO-NF@Cu can give 100% HMF conversion with a 99.6% FDCA yield and 99.3% FDCA FE at a potential of 1.62 V (*vs.* RHE) in 45 min. Moreover, CO_2RR and HMFOR can be coupled together in an integrated flowing cell with CuO-NF@Cu as the electrocatalyst in both the anode and cathode (Fig. 1). A stable current density up to 188.8 mA cm^{-2} at a cell voltage of 2.75 V can be obtained, along with a FDCA FE up to 96.6% and a C_2H_4 FE up to 74.5%. The excellent performance of the Cu-based nanoflower electrocatalyst demonstrates great promise for the large scale cyclic utilization of CO_2 resources generated from coal or oil and biomass valorization, facilitated by renewable electric energy from wind, solar, *etc.*

Results and discussion

Catalyst preparation and characterization

In this study, Cu nanoflower sheet catalysts were grown over foam Cu. Detailed catalyst preparation methods are given in the ESI† and are illustrated in Fig. S1 (in the ESI†). The mor-

phology and microstructure of the catalyst in different stages in Fig. S1† are characterized by SEM and shown in Fig. S2.† Without stirring, the yellow surface of the pristine Cu foam turned blue in 10 min, indicating the formation of $Cu(OH)_2$ over the Cu foam. The SEM images in Fig. S2a and b† show that the surface of the Cu foam turned from smooth to rough and $Cu(OH)_2$ nanorods uniformly covered the surface of the Cu foam ($Cu(OH)_2$-NR@Cu). After 20 min, the surface turned dark blue, indicating that partial $Cu(OH)_2$ had dehydrated to CuO. The SEM images showed that CuO nucleated and formed a small amount of CuO nanoflowers over the $Cu(OH)_2$ nanorods (CuO/$Cu(OH)_2$-NR@Cu, Fig. S2c†). Vigorous stirring in the catalyst preparation can accelerate this transformation and a black surface can be found in 20 min with stirring in the catalyst preparation, implying that a majority of the Cu foam surface is covered by CuO. The SEM image in Fig. S2d† shows that CuO nanoflowers covered the whole surface of the Cu foam (CuO-NF@Cu). Under alkaline conditions, the inorganic polymerization reactions of $Cu(OH)_2$, CuO/$Cu(OH)_2$, and CuO are as follows.

$$Cu + 4OH^- + (NH_4)_2S_2O_8 \rightarrow Cu(OH)_2 + 2NH_3(g) + 2SO_4^{2-} + 2H_2O \quad (1)$$

$$Cu(OH)_2 \leftrightharpoons CuO + H_2O \quad (2)$$

At first, Cu atoms on the Cu foam surface dissolved into Cu^{2+} in the presence of $(NH_4)_2S_2O_8$. In the presence of OH^-, partial Cu^{2+} formed $Cu(OH)_2$ and deposited on the Cu foam surface ($Cu(OH)_2$@Cu, Fig. S2b†). With the reaction time prolonged to 20 min and Cu^{2+} saturated in the solution, $Cu(OH)_2$ dehydrated to CuO, which is thermodynamically favorable. The formed CuO nucleated and grew on the surface with the production and dehydration of $Cu(OH)_2$. Depending on the rates of formation and dehydration of $Cu(OH)_2$, a mixture of CuO and $Cu(OH)_2$ can exist on the surface (CuO/$Cu(OH)_2$@Cu, Fig. S2c†). Stirring during the reaction accelerated the nucleation rate until the surface oxygen content no longer increased, indicating that the surface was completely covered by the oxide layer (Fig. S2d†). Finally, vertically arranged and densely stacked CuO nanoflowers (CuO-NF@Cu) were synthesized. This method not only prevents the increase of contact resistance between the nanorods/flowers and the conductive substrate but also interferes with the diffusion of the electrolyte, thereby improving the catalytic performance.

Further SEM observations and analysis of the CuO-NF@Cu were conducted and are shown in Fig. 2. An EDS elemental analysis of the nanoflowers and the EDS elemental spectra showed that the Cu and O elements are evenly distributed on the nanoflowers, with an atomic ratio of oxygen to copper close to 1 : 1, indicating the successful preparation of CuO-NF@Cu (Fig. 2b and c). Meanwhile, an EDS elemental analysis of the nanoflowers on CuO/$Cu(OH)_2$@Cu showed that the atomic ratio of oxygen to copper was also close to 1 : 1 (Fig. S3†), confirming that CuO nanoflowers nucleated and grew on the $Cu(OH)_2$ nanorods. High-magnification SEM and HRTEM in Fig. 3a and b indicate that the CuO nanoflowers are composed of ultra-thin CuO nanosheets, with an average width of *ca.* 200 nm. The thickness of the nanosheets was measured with atomic force microscopy (AFM) and found to be *ca.* 4.5 nm (Fig. 3c). The ultra-thin nanosheets of CuO-NF@Cu provide more catalytic active sites during the electrocatalytic process. The above characterization demonstrated the successive preparation of CuO nanoflowers with nanosheets over Cu foam.

The crystal structure of the catalysts was determined by X-ray diffraction (XRD) and is shown in Fig. S4.† All the catalysts exhibit three high-intensity diffraction peaks at 43.316°, 50.448°, and 74.142°, corresponding to the Cu (111), (200), and (220) planes (Fig. S4a†), respectively (JCPDS Card No. 04-0836), indicating that $Cu(OH)_2$ nanorods and CuO nanoflowers directly grew on the surface of the Cu foam (Fig. S4b–d†). The XRD pattern of $Cu(OH)_2$-NR@Cu in Fig. S4b† exhibits typical diffraction peaks at 34.061°, 39.800°and 53.210° which are respectively assigned to the (002), (130) and (150) planes of the orthorhombic crystal phase of $Cu(OH)_2$ (JCPDS Card No. 13-0420). The XRD pattern of CuO/$Cu(OH)_2$@Cu in Fig. S4c† shows typical diffraction peaks at 36.636° and 42.558°, which correspond to the (002) and (111) planes of the orthorhombic crystal phase of CuO (JCPDS Card No. 80-1917), in addition to the diffraction peaks assigned to $Cu(OH)_2$. For the CuO-NF@Cu catalyst, no other phases were observed except for Cu (JCPDS Card No. 04-0836) and CuO (JCPDS Card No. 80-1917), as shown in Fig. S4d.†

To further investigate the surface chemical composition and valence state of the catalyst, XPS analysis was performed and is given in Fig. S5.† Fig. S5a† shows the XPS spectrum of the CuO-NF@Cu catalyst, in which the characteristic peaks of copper, oxygen, and carbon can be clearly observed. According to the XPS quantitative analysis of the CuO-NF@Cu catalyst, the ratio of oxygen to copper in the catalyst is 1.15 : 1, which is almost consistent with the ratio of 1.08 : 1 measured by inductively coupled plasma optical emission spectroscopy (ICP-OES). In the high-resolution Cu 2p spectrum of the catalyst, the two peaks of Cu $2p_{1/2}$ and Cu $2p_{3/2}$ are located at 952.90 eV and 933.11 eV, respectively (Fig. S5b,† bottom), and are caused by elemental copper. The strong shake-up peaks at 943.65 eV and 963.00 eV indicate the presence of Cu^{2+} (Fig. S5b,† top) and cannot be found in the spectrum of the copper foam. The main peak of Cu $2p_{3/2}$ can be further divided into two peaks, those of Cu^{2+} from CuO at 935.47 eV and Cu^0 at 933.82 eV, because of the inevitable minor amount of Cu remaining unreacted in the process (Fig. S5c†). In addition, the O 1s spectrum (Fig. S5d†) can be divided into two peaks, which belong to the Cu–O bond of CuO at 529.44 eV and a peak at 531.26 eV attributed to hydroxyl groups adsorbed on the surface.

Cathodic electrochemical CO_2 reduction to ethylene

CuO-NF@Cu was used as the working electrode for electrochemical CO_2 reduction, with an Ag/AgCl electrode as the

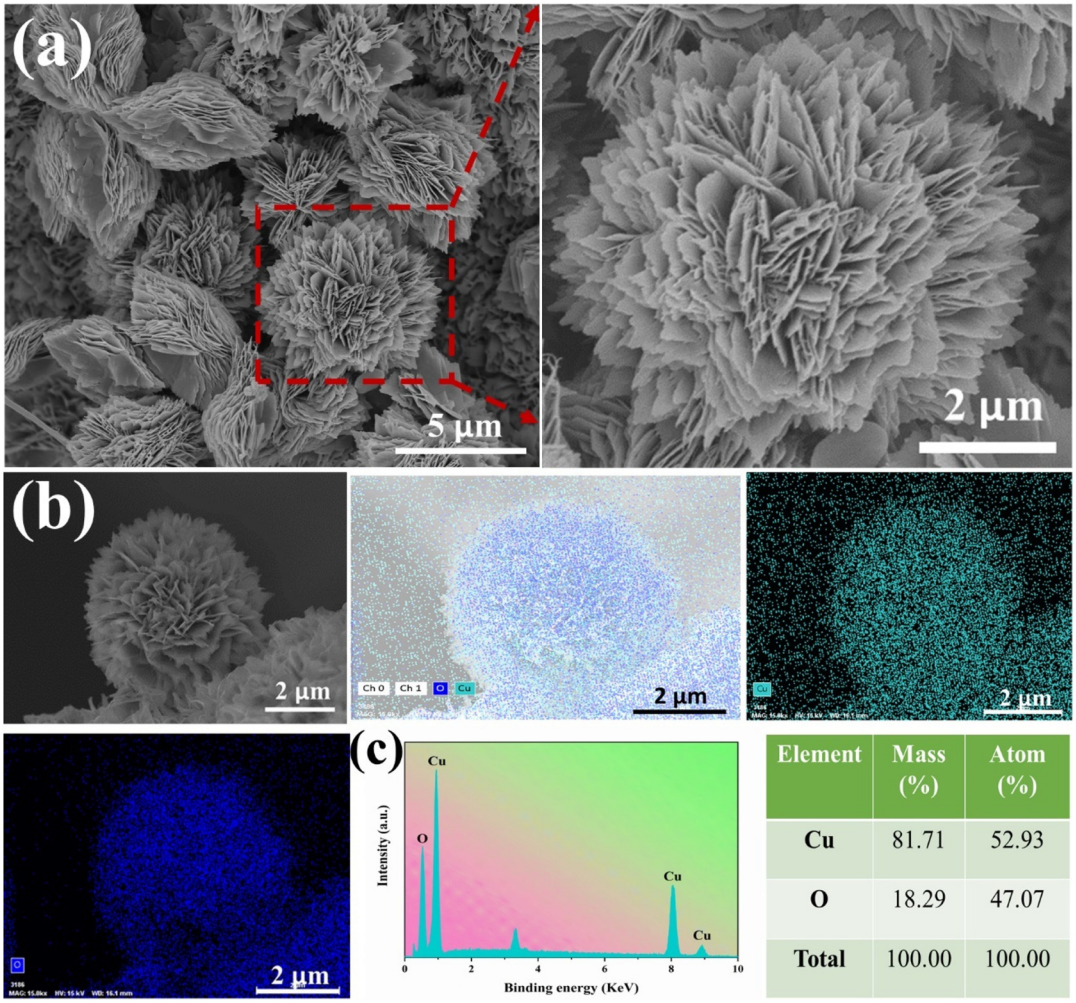

Element	Mass (%)	Atom (%)
Cu	81.71	52.93
O	18.29	47.07
Total	100.00	100.00

Fig. 2 (a) SEM images of CuO-NF@Cu, (b) elemental mapping images of CuO-NF@Cu, (c) EDS spectrum of CuO-NF@Cu.

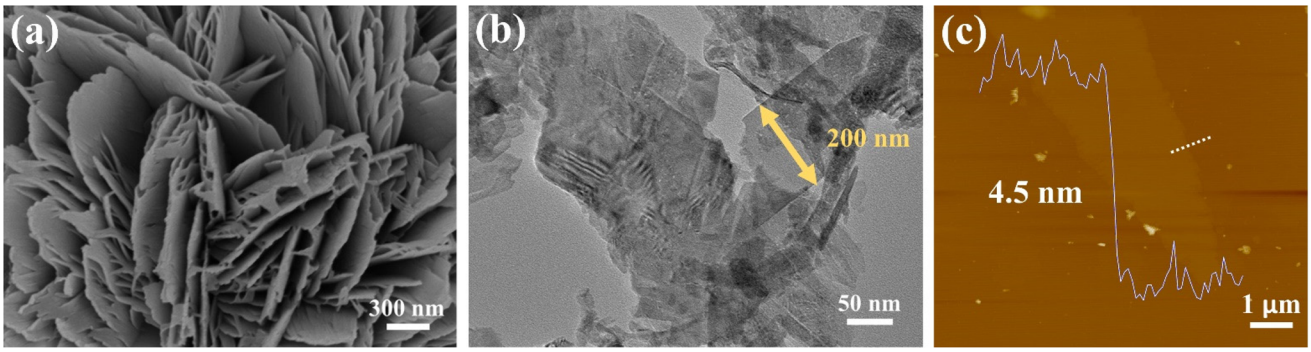

Fig. 3 (a) High-magnification SEM and (b) HRTEM images of CuO-NF@Cu at different magnifications; the CuO flakes are about 200 nm in width and 6 nm in thickness. (c) AFM image of the CuO-NF@Cu and the corresponding height profile from the dashed line.

reference electrode and a platinum foil as the counter electrode. *In situ* constant current reduction was performed at −0.95 V (*vs.* RHE) under a flowing CO_2 atmosphere. The current decreased sharply in the first 6 min (360 seconds) of electrochemical reduction from *ca.* 182.0 mA cm^{-2} to *ca.* 104.5 mA cm^{-2} (Fig. 4a, middle) and the black surface of the CuO-NF@Cu catalyst quickly turned reddish-brown (Fig. S6†), indicating that CuO in CuO-NF@Cu can be quickly reduced. To check the composition of the reduced CuO-NF@Cu, X-ray diffraction (XRD) over CuO-NF@Cu and reduced CuO-NF@Cu

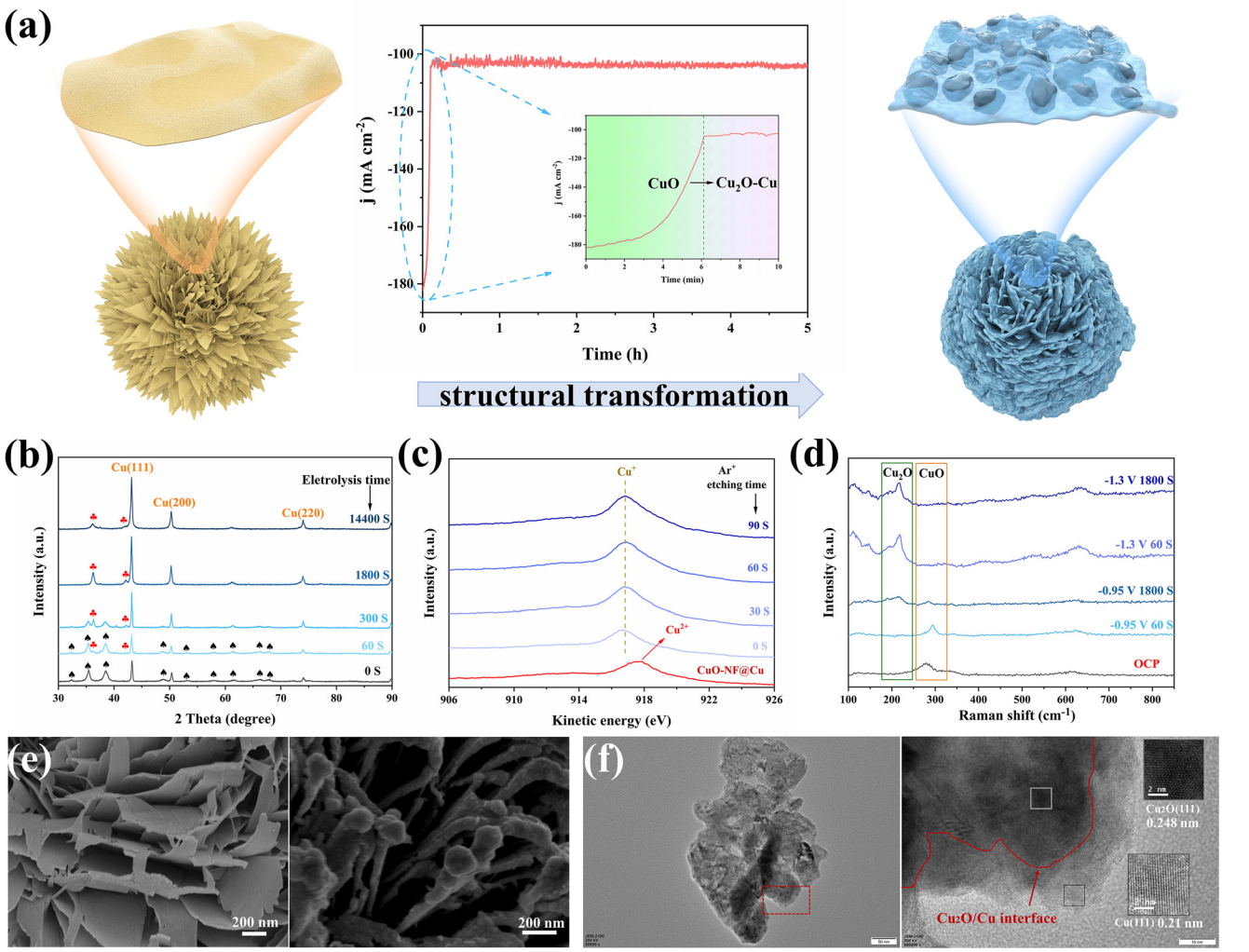

Fig. 4 (a) Schematic illustration of morphology changes during the electrochemical reduction of CuO-NF@Cu, (b) XRD patterns of CuO-NF@Cu at different reduction times, (c) Cu LMM Auger spectra of CuO-NF@Cu and Cu_2O/Cu-NF@Cu with different Ar^+ etching times, (d) *in situ* Raman spectra of Cu_2O/Cu-NF@Cu in different conditions, (e) SEM images of fresh CuO-NF@Cu and Cu_2O/Cu-NF@Cu, (f) TEM and HRTEM images of Cu_2O/Cu-NF@Cu.

at different reduction times was conducted and the results are shown in Fig. 4b. The XRD pattern indicates that, besides Cu diffraction peaks, only CuO diffraction peaks were observed in CuO-NF@Cu (spade marks in Fig. 4b). After 60 seconds of electrochemical reduction, diffraction peaks attributed to Cu_2O begin to appear (red club marks in Fig. 4b). After 300 seconds of electrochemical reduction, the CuO peak completely disappears, while the Cu_2O peak still exists, even if the reduction time is extended to 1800 seconds (0.5 h) and 14 400 seconds (4 h). These results implied that surface CuO in CuO-NF@Cu can be reduced into Cu_2O which is stable under current reduction conditions. Thus, the cathode catalyst is named Cu_2O/Cu-NF@Cu in the following text.

To check the surface and subsurface Cu valence states of CuO-NF@Cu and Cu_2O/Cu-NF@Cu, X-ray photoelectron spectroscopy (XPS) and Auger electron spectroscopy (AES) were conducted with different times of Ar^+ etching over Cu_2O/Cu-NF@Cu, as shown in Fig. 4c and Fig. S7, S8.† The Cu_2O/Cu-NF@Cu sample was obtained by 2 hours of electrochemical reduction under the above-mentioned conditions to ensure that its structure was the same as the cathode used in the long-time CO_2RR. In CuO-NF@Cu, the Cu LMM Auger peak at 917.4 eV and the typical satellite peaks can be attributed to Cu^{2+} species. In the XPS spectra of Cu_2O/Cu-NF@Cu and Ar^+ etched Cu_2O/Cu-NF@Cu with etching times from 0–90 seconds, no Cu^{2+} but only Cu^+ peaks were found, indicating that the original Cu^{2+} species in CuO-NF@Cu were completely reduced to Cu^+ after electrolysis. The Cu LMM spectrum shows that Cu^+ species can exist in Cu_2O/Cu-NF@Cu even after 90 s of Ar^+ etching (estimated etching depth of 30 nm), which can completely exclude the surface oxide layer formed by air oxidation (usually <5 nm). Meanwhile, the peaks belonging to the Cu and O elements are compared in Fig. S7 and S8†: the Cu peak intensity increased and the O peak intensity decreased

with detection depth increasing, indicating that the original CuO phase was generated over the Cu foam surface. Further *in situ* Raman spectroscopy was performed to identify the valence of Cu during electrolysis (Fig. 4d). The peaks of Raman shifts at 287, 337, and 622 cm^{-1} belong to CuO under open circuit potential (OCP) and can be clearly observed. When Cu_2O/Cu-NF@Cu was reduced at −0.95 V (*vs.* RHE) for 60 s, the characteristic peak belonging to CuO became weakened and the peak belonging to Cu_2O began to appear.[47] After 1800 s, the CuO peak completely disappeared but the Cu_2O peak remained. At higher potential (−1.3 V *vs.* RHE in Fig. 4d), Cu^+ can also be retained even after undergoing long-time electrochemical reduction. Therefore, it can be concluded that Cu^+ species will be preserved during the electrochemical CO_2RR process.

Morphology changes before and after electrochemical reduction were characterized by SEM and TEM. As shown in Fig. 4e and Fig. S9,† SEM images of electrochemically reduced CuO-NF@Cu indicate that the vertically arranged and densely stacked laminated nanostructures are retained. However, the flakes are no longer composed of CuO nanosheets but nanoparticles. Each ultrathin nanosheet transformed into a thicker nanosheet composed of small nanoparticles.

The HRTEM images provide direct evidence for the self-evolution of nanoflakes in CuO-NF@Cu to nanoparticles in Cu_2O/Cu-NF@Cu, as shown in Fig. 3b and Fig. S10.† The complete Cu_2O/Cu-NF@Cu nanoflakes were reduced and restructured to Cu_2O and Cu, resulting in a large number of grain boundary interfaces (GBs) between Cu_2O and Cu (Fig. 4f). The large Cu particles were wrapped by Cu_2O facets and a Cu (111) plane with a lattice spacing of 0.21 nm was observed on the larger Cu particles, while a Cu_2O (111) plane with a lattice spacing of 0.248 nm was observed around the Cu particles. As a result, a large number of Cu_2O (111) facets and Cu (111) particles provide rich Cu_2O (111)/Cu (111) (Cu^+/Cu^0) interfaces in the Cu_2O/Cu-NF@Cu nanoflakes.

Electrochemical CO_2 reduction over the Cu_2O/Cu-NF@Cu electrode was evaluated at atmospheric pressure using a three-electrode H-type electrolytic cell setup. Fig. 5a shows the LSV curves of Cu_2O/Cu-NF@Cu in 0.5 M KCl water solution saturated with N_2 or CO_2 at a scan rate of 2 mV s^{-1} (methods in ESI†). Much higher current was observed in a flowing CO_2 atmosphere than in N_2 atmosphere at all scan potentials, demonstrating the significant CO_2RR performance of Cu_2O/Cu-NF@Cu. The reduction products were then detected and the liquid products were mainly ethanol and formate, with a small amount of acetate (Fig. S11†). In the gas products, C_2H_4 and H_2 were the main reduction products (Fig. S12†). Over Cu_2O/Cu-NF@Cu at various potentials, the highest Faraday efficiencies (FE) of 70% for C_2H_4 and 59.6% for C_2H_4 selectivity were obtained at −0.95 V (Fig. 5b, Fig. S13 and Table S1 in ESI†). Additionally, the FE_{H_2} was only 17.5% at −0.95 V over Cu_2O/Cu-NF@Cu. The high proportion of C_{2+}/C_1 (CO, CH_4, formate) in the CO_2RR products further confirms the kinetic advantage of C_2H_4 and C_{2+} formation over Cu_2O/Cu-NF@Cu (Fig. 5c). According to previous research, the performance observed in stability tests of OD-Cu[48,49] catalysts has consistently failed to meet satisfactory levels. Long-term electrolysis at −0.95 V (*vs.* RHE) over Cu_2O/Cu-NF@Cu (Fig. 5d) showed a stable *i–t* curve with a current density of 104.5 mA cm^{-2} and high C_2H_4 FE ($FE_{C_2H_4} \approx 70\%$) over 45 hours.

After long-term testing, XRD characterization of the recovered Cu_2O/Cu-NF@Cu catalyst indicated that the characteristic peak of Cu_2O was retained in the spectrum (Fig. S14†). XPS analysis showed that Cu_2O/Cu-NF@Cu retained a similar Cu/Cu^+ interface structure and Cu^+ content in the subsurface (Fig. S15†). SEM images showed that the nanoflakes were still stacked densely and orderly after 45 hours of electrolysis without any aggregation, and only a slight increase in the thickness of nanoflakes was observed (Fig. S16a and b†). HRTEM images showed that the Cu_2O/Cu (Cu/Cu^+) interfaces in the Cu_2O/Cu-NF@Cu catalyst were preserved (Fig. S16c and d†), indicating the excellent stability of the Cu_2O/Cu-NF@Cu catalyst compared to previous reported catalytic systems (Table S2†). The stable Cu/Cu^+ interfaces are believed to be active catalytic sites for C_2H_4 formation and the detailed mechanism can be found in previous reports.[50,51] Moreover, this prepared CuO-NF@Cu is more stable than those previously reported. This work provides a feasible procedure for preparing a stable Cu/Cu^+ interface-containing nanocatalyst and verifies its effectiveness in CO_2RR and HMFOR.

Anodic high efficiency oxidation of HMF to FDCA

To investigate the activity of the prepared CuO-NF@Cu catalyst in anodic HMF electrochemical oxidation, a series of electrochemical tests was conducted in a three-electrode setup. The linear sweep voltammetry (LSV) curves of CuO-NF@Cu in 0.1 mol L^{-1} KOH solution with and without HMF are given in Fig. S17.† With HMF, an obviously higher current can be observed than that without HMF under the studied potentials. The copper foam has no effect on the anodic HMF oxidation (Fig. S18†). The electrocatalytic oxidation of HMF to FDCA involves two possible oxidation pathways (Fig. S19†). With constant potential oxidation of HMF at 1.62 V (*vs.* RHE), the concentration changes of HMF, intermediate products, and FDCA detected by HPLC are shown in Fig. 6a and b. The results show that the HMF concentration in the reaction medium decreased continuously with a concomitant increase of FDCA, along with the passed charges increasing during reaction. Small amounts of intermediate products, such as HMFCA and DFF, were also detected. FFCA was detected as the main accumulated intermediate product during electrolysis, indicating that the oxidation of FFCA to FDCA is the rate-determining step. The current density decreased from 70.3 mA cm^{-2} in the beginning of reaction to 8.3 mA cm^{-2} with the decrease of HMF concentration in the reaction medium (Fig. S20†). The passed charge was calculated during electrocatalysis and when 116 C electrons were passed in 45 min, 100% HMF conversion with 99.6% FDCA selectivity and 99.3% FE of FDCA were obtained at 1.62 V (*vs.* RHE). The HMF conversion and FDCA yield of the CuO-NF@Cu electrode were almost directly proportional to the passed charge (Fig. 6b and S21†).

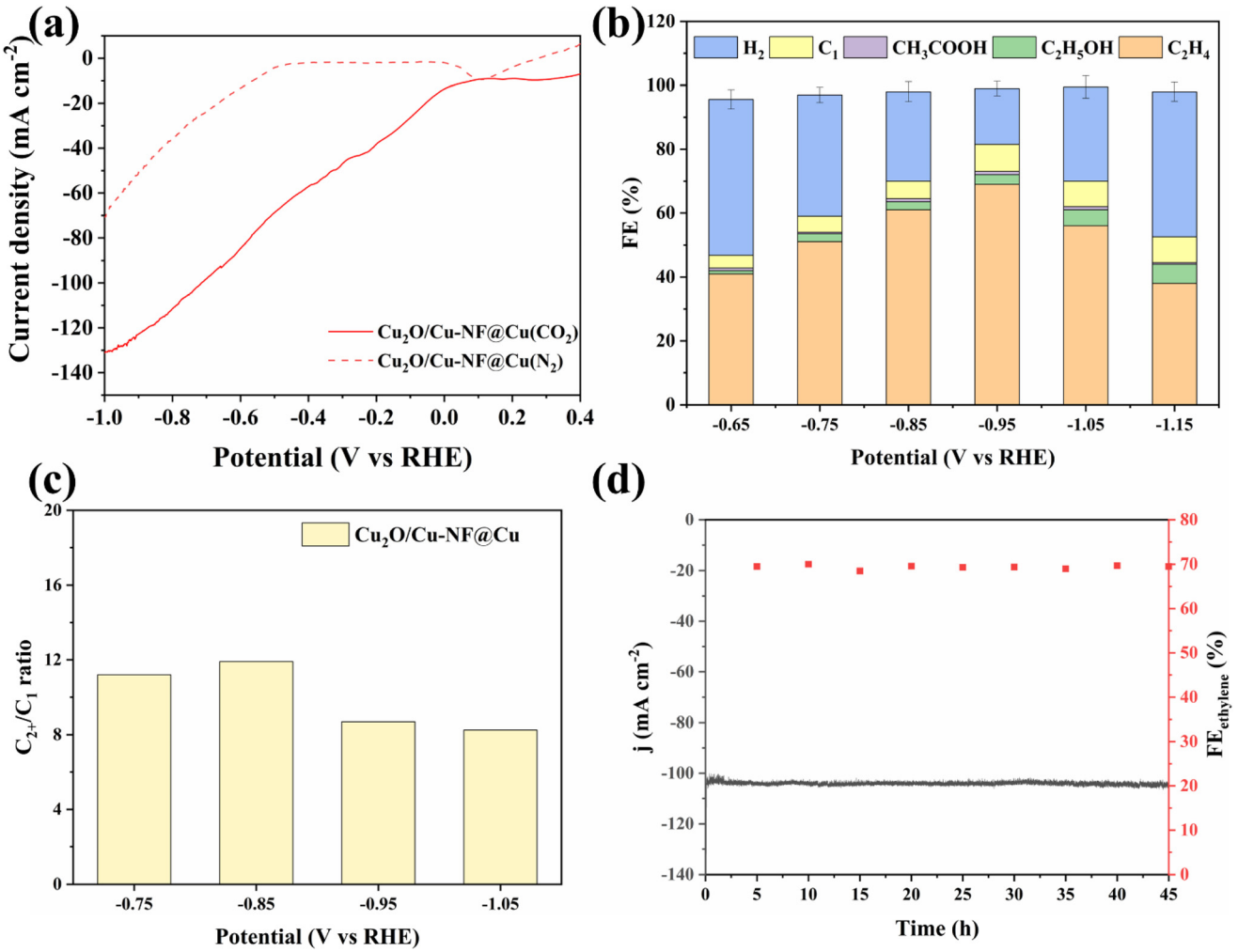

Fig. 5 (a) LSV curves over Cu_2O/Cu-NF@Cu in Ar and CO_2 saturated KCl electrolyte, (b) FEs of products over Cu_2O/Cu-NF@Cu, (c) C_{2+}/C_1 ratios for CO_2RR products, (d) long-term stability test of 45 h at −0.95 V *vs.* RHE for Cu_2O/Cu-NF@Cu.

The high FE of FDCA encouraged us to check its dependence on the potential; the results in Fig. 6c show that the high FDCA FE can be maintained over a wide voltage range but started to decrease when the bias exceeded 1.67 V (*vs.* RHE) due to the competing OER. To study the stability of CuO-NF@Cu, five consecutive cycles of HMF oxidation were performed at a potential of 1.62 V and are shown in Fig. 6d. High and stable FDCA yield and FE were observed in the 5 recycle tests. Compared with previously reported catalysts (ESI Table S3†), CuO-NF@Cu exhibits comparable performance in the electrochemical oxidation of HMF into FDCA.

Furthermore, the crystal structure, morphology, composition, and element distribution of CuO-NF@Cu after five consecutive electro-oxidation cycles of HMF were investigated by XRD, SEM, EDS mapping, and XPS. XRD patterns (Fig. S22†) and SEM images (Fig. S23†) showed an almost identical crystal lattice and morphology of CuO-NF@Cu before and after long-term electrolysis. Moreover, the composition and element distribution of CuO-NF@Cu (Fig. S24†) and binding energy of Cu 2p (Fig. S25†) did not show significant changes after long-term electrocatalysis. All these results demonstrate the high stability of CuO-NF@Cu, which is crucial for future industrial applications.

Simultaneous cathodic CO_2RR and anodic HMFOR over Cu-based nanoflower sheets

Encouraged by the excellent CO_2RR and HMFOR performances of the Cu-based nanoflower sheets, we pursued coupling these two half-reactions in one cell. To evaluate the potential application of the catalyst in an industrial-scale reactor, we measured their catalytic performance in a flow cell. CuO-NF@Cu was used directly as the anode electrode. In the cathode, the catalyst CuO-NF@Cu was first sprayed onto carbon paper (Sigracet 39BB) with a gas diffusion layer (GDL, CuO-NF@GDL), followed by constant current cathodic reduction to obtain Cu_2O/Cu-NF@GDL. The detailed synthesis method is given in the ESI† ('Electrocatalysis experiments' section). The prepared CuO-NF@GDL were characterized by

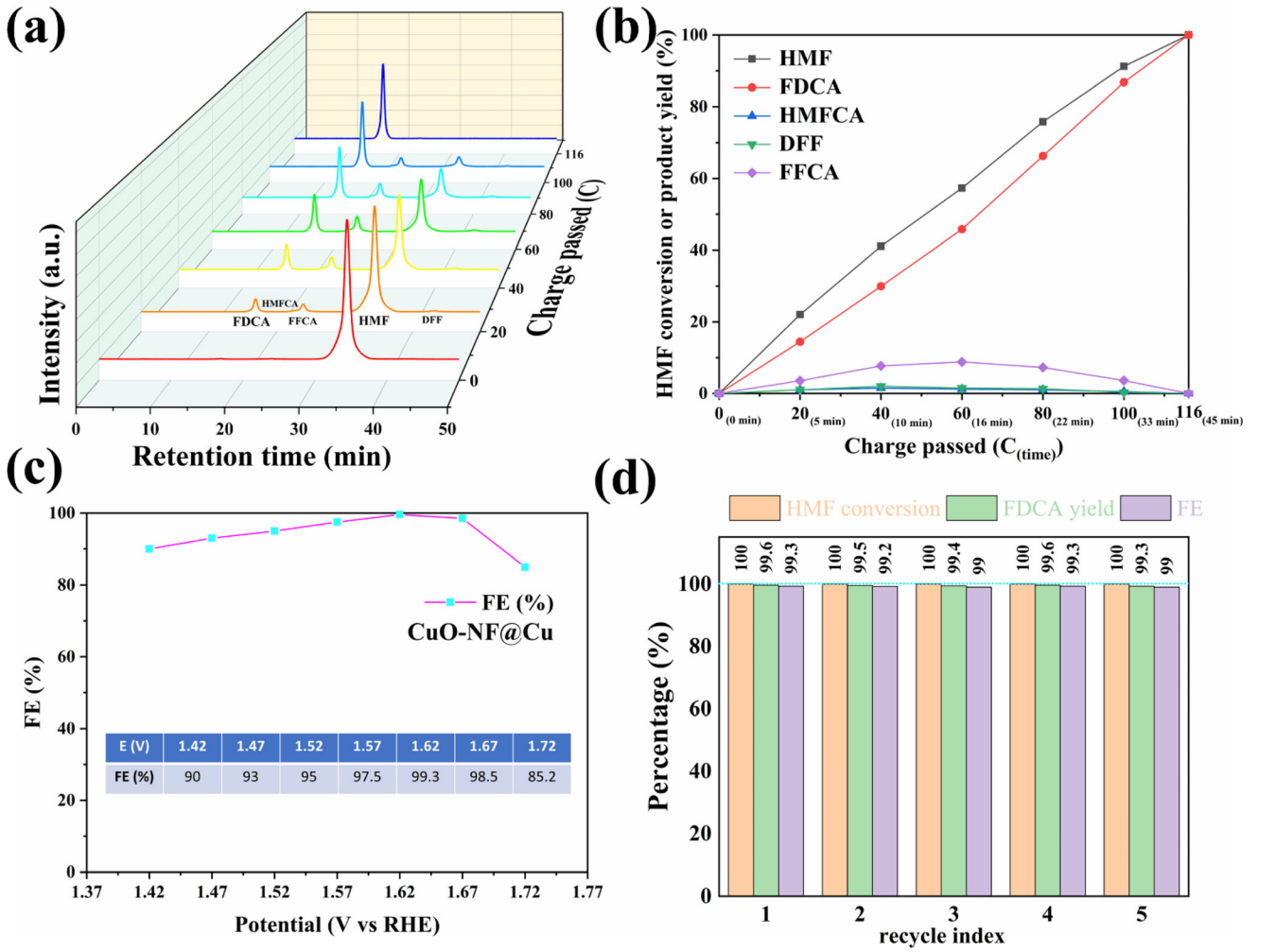

Fig. 6 (a) HPLC spectra of HMF reaction solution *vs.* passed charges during reaction, (b) HMF conversion and products yields *vs.* passed charges during reaction, (c) FE of FDCA at varied potentials, (d) recycling tests of CuO-NF@Cu.

SEM (Fig. S26 and S27†) and the results indicate that CuO-NF@GDL has same nanostructure as CuO-NF@Cu. During the flowing CO_2RR-HMFOR process, the CuO-NF on GDL was reduced to Cu_2O/Cu-NF (Cu_2O/Cu-NF@GDL). After the reaction, the Cu_2O/Cu-NF@GDL was recovered and characterized by SEM and HRTEM. Results show that Cu_2O/Cu-NF@GDL has a similar nanoflower structure (Fig. S28 and S29†) to Cu_2O/Cu-NF@Cu (Fig. 4e, f and Fig. S9, S10†).

The coupled CO_2RR-HMFOR over Cu-based electrode was tested in a flowing setup, as shown in Fig. 7. The cathode (CuO-NF@GDL) and anode (CuO-NF@Cu) were connected to conductive copper tapes so that they could connect to an external electrochemical workstation. A bipolar membrane and the two electrodes were combined using polytetrafluoroethylene spacers so that a liquid electrolyte could be introduced into the chambers between the anode and the membrane, as well as between the membrane and the cathode. In the CO_2RR compartment, gaseous CO_2 passed through the gas chamber at the back side of CuO-NF@GDL with a constant flow rate of 15 mL min^{-1}. 100 mL of circular 0.5 M KCl aqueous solution was used as the catholyte and 2 M KOH aqueous solution mixed with or without 10 mM HMF was used as the anolyte. The electrolyte flow rates at both sides were kept at 10 mL min^{-1} during the reaction. LSV tests in Fig. 8a show that there is an obviously higher current density in coupled CO_2RR-HMFOR than in CO_2RR-OER (without HMF), HMFOR-HER (without CO_2) or HER-OER (without CO_2 and HMF), indicating the overall thermodynamic advantage of the CO_2RR-HMFOR process over Cu-based nanoflower sheets. Specifically, coupled CO_2RR-HMFOR provided a current density of 100 mA cm^{-2} at a cell voltage of 2.31 V, which was 790 mV lower than the voltage of CO_2RR-OER (3.1 V). At cell voltages of 2.5, 2.75, and 3 V, the timed-current curves showed high current densities of 134.5, 188.8 and 245.1 mA cm^{-2} (Fig. 8b), respectively. The corresponding $FE_{C_2H_4}/FE_{FDCA}$ values in coupled CO_2RR-HMFOR were calculated to be 55.6%/85.5%, 74.5%/96.6%, and 58.6%/88.3%, respectively (Fig. 8c). The stability test of the Cu-based nanoflower sheet catalysts in coupled CO_2RR-HMFOR gave a highly stable current density of about 190.0 ± 5.2 mA cm^{-2} within 5 hours and the $FE_{C_2H_4}$/

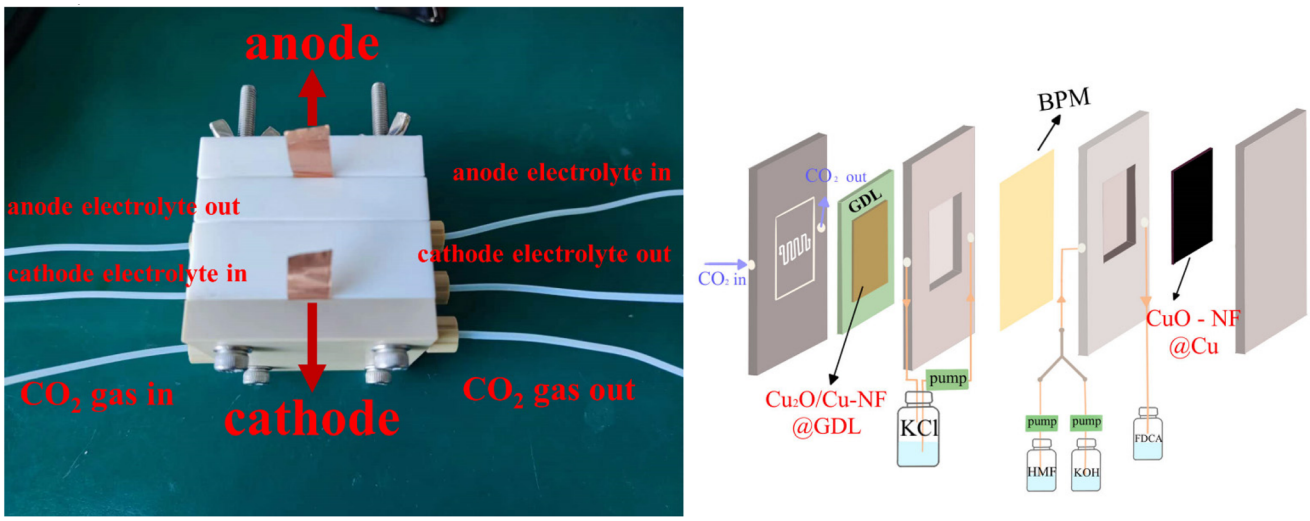

Fig. 7 Photo and schematic illustration of the used flow cell.

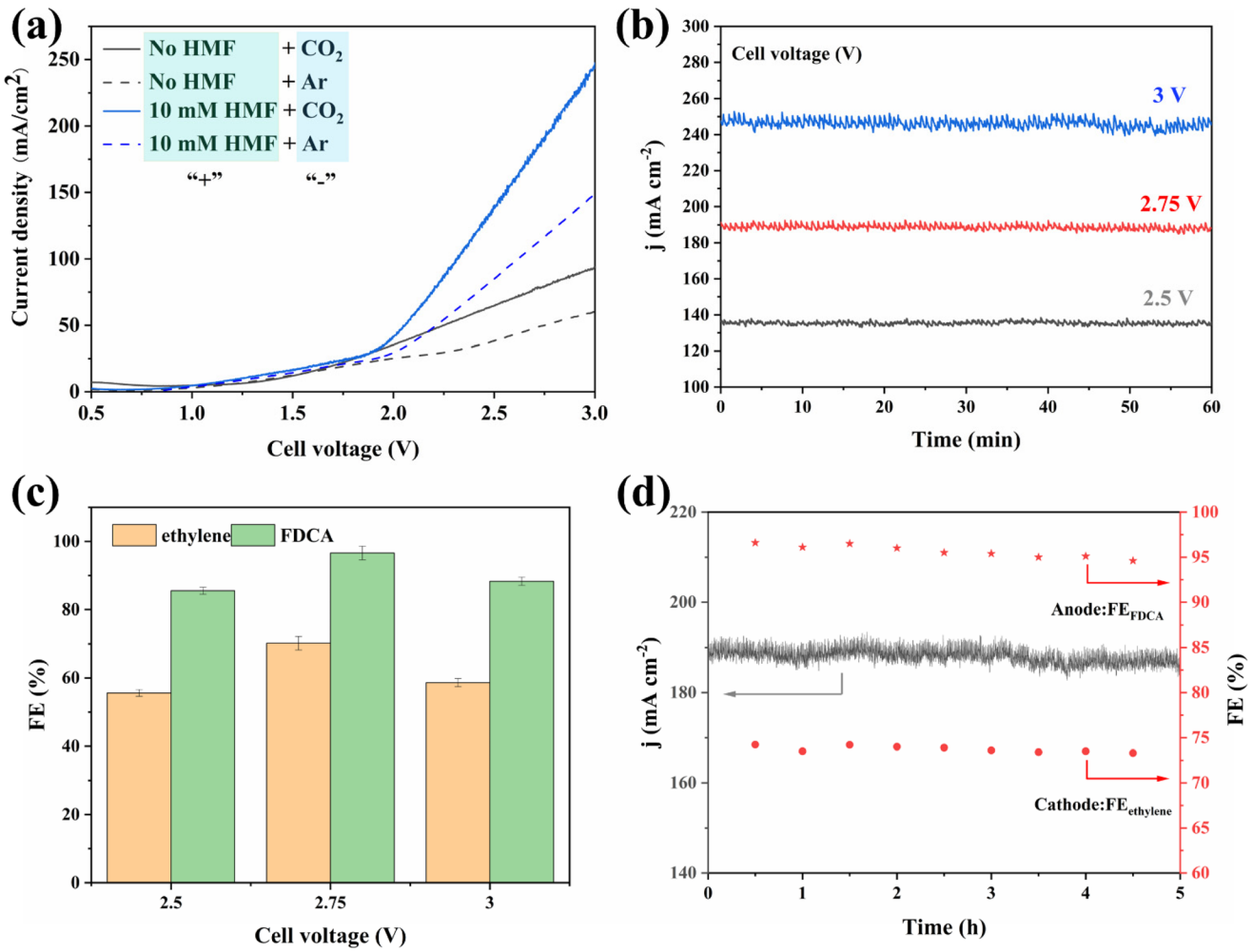

Fig. 8 (a) LSV curves recorded in two-electrode setup. "+": anodic compartment; "–": cathodic compartment. (b) Chronoamperometry curves under different cell voltages, (c) corresponding FE for CO_2RR-HMFOR couple under different cell voltages, (d) stability test of Cu-based nanoflower sheets in CO_2RR-HMFOR coupled reaction under a cell voltage of 2.75 V.

FE_{FDCA} values were maintained at *ca.* 71 ± 3.8%/93 ± 3.6% (Fig. 8d). The anode CuO-NF@Cu in the coupled reaction was recovered after 5 h and characterized by SEM; the results (Fig. S30†) show that the recovered CuO-NF@Cu maintained its original nanostructure, as shown in Fig. 2 and 3. Thus, the high FE of FDCA and C_2H_4 in coupled CO_2RR-HMFOR can be attributed to the stable nanostructure of the CuO nanoflower sheets in CuO-NF@Cu and the stable Cu/Cu^+ interface in Cu_2O/Cu-NF@Cu (Fig. S9 and S10†).

Conclusions

In this work, foam Cu was easily modified to a nanoflower CuO-covered Cu foam catalyst, where CuO is composed of a stable structure of nanosheets. In CO_2RR, CuO-NF@Cu can be quickly reduced to a nanoflower-shaped Cu_2O/Cu-NF@Cu, which has a stable nanoparticle structure and stable Cu^+/Cu interface. At a reduction potential of −0.95 V (*vs.* RHE), a high C_2H_4 FE up to 70% with a current density above 100 mA cm^{-2} can be obtained. In HMFOR, CuO-NF@Cu shows excellent catalytic activity in the oxidation of HMF into FDCA. At a constant potential of 1.62 V (*vs.* RHE) and passed charge of 116 C, the FE of FDCA reached 99.3%. In coupled CO_2RR-HMFOR with the above Cu-based nanoflower electrocatalysts, a current density up to 188.8 mA cm^{-2} at a cell voltage of 2.75 V can be obtained. Moreover, FE vales of FDCA and C_2H_4 up to 74.5% and 96.6%, respectively, in the coupled CO_2RR-HMFOR were achieved. The microstructure of the Cu-based nanoflower catalyst maintained stability and gave above 180.0 mA cm^{-2} current density within 5 h of testing. This work shows that an easily prepared Cu-based catalyst can be used as a highly efficient electrocatalyst to achieve high-value products by the oxidation of biomass platform compounds in the anode and the reduction of CO_2 into high-value C_2H_4 in the cathode. With the development of efficient electrocatalysts, renewable energy can be used to achieve the resource utilization of CO_2 produced from fossil resources while also upgrading renewable biomass resources.

Conflicts of interest

There are no conflicts to declare.

Acknowledgements

This work was financially supported by the National Natural Science Foundation of China (Grant 21805145, 22002065), the Department of Science and Technology of Shandong Province (ZR2020QB060, ZR2019BB068), and the funding support from Qilu University of Technology (Shandong Academy of Sciences) (2022PY072). Science and Technology Plan Project of Shandong Provincial University (J12LA02), Program for Scientific Research Innovation Team in Colleges and Universities of Shandong Province.

References

1 J. P. Gattuso, A. Magnan, R. Bille, W. W. Cheung, E. L. Howes, F. Joos, *et al.*, Oceanography. Contrasting futures for ocean and society from different anthropogenic CO(2) emissions scenarios, *Science*, 2015, **349**(6243), aac4722.
2 C. Hepburn, E. Adlen, J. Beddington, E. A. Carter, S. Fuss, N. Mac Dowell, *et al.*, The technological and economic prospects for CO(2) utilization and removal, *Nature*, 2019, **575**(7781), 87–97.
3 H. S. Shafaat and J. Y. Yang, Uniting biological and chemical strategies for selective CO2 reduction, *Nat. Catal.*, 2021, **4**(11), 928–933.
4 P. Zhu and H. Wang, High-purity and high-concentration liquid fuels through CO2 electroreduction, *Nat. Catal.*, 2021, **4**(11), 943–951.
5 Y. Li, C.-Z. Huo, H.-J. Wang, Z.-X. Ye, P.-P. Luo, X.-X. Cao, *et al.*, Coupling CO2 reduction with CH_3OH oxidation for efficient electrosynthesis of formate on hierarchical bifunctional CuSn alloy, *Nano Energy*, 2022, **98**, 107277.
6 S. N. Sun, L. Z. Dong, J. R. Li, J. W. Shi, J. Liu, Y. R. Wang, *et al.*, Redox-Active Crystalline Coordination Catalyst for Hybrid Electrocatalytic Methanol Oxidation and CO(2) Reduction, *Angew. Chem., Int. Ed.*, 2022, **61**(34), e202207282.
7 Q. Liu, J. Lin, H. Cheng, L. Wei and F. Wang, Simultaneous co-Photocatalytic CO(2) Reduction and Ethanol Oxidation towards Synergistic Acetaldehyde Synthesis, *Angew. Chem., Int. Ed.*, 2023, **62**(13), e202218720.
8 X. She, Y. Wang, H. Xu, S. C. E. Tsang and S. P. Lau, Challenges and Opportunities in Electrocatalytic CO(2) Reduction to Chemicals and Fuels, *Angew. Chem., Int. Ed.*, 2022, **61**(49), e202211396.
9 D. Li, K. Yang, J. Lian, J. Yan and S. Liu, Powering the World with Solar Fuels from Photoelectrochemical CO 2 Reduction: Basic Principles and Recent Advances, *Adv. Energy Mater.*, 2022, **12**(31), 2201070.
10 J. Gu, S. Liu, W. Ni, W. Ren, S. Haussener and X. Hu, Modulating electric field distribution by alkali cations for CO2 electroreduction in strongly acidic medium, *Nat. Catal.*, 2022, **5**(4), 268–276.
11 J. Y. T. Kim, P. Zhu, F.-Y. Chen, Z.-Y. Wu, D. A. Cullen and H. Wang, Recovering carbon losses in CO2 electrolysis using a solid electrolyte reactor, *Nat. Catal.*, 2022, **5**(4), 288–299.
12 J. Timoshenko, A. Bergmann, C. Rettenmaier, A. Herzog, R. M. Arán-Ais, H. S. Jeon, *et al.*, Steering the structure and selectivity of CO2 electroreduction catalysts by potential pulses, *Nat. Catal.*, 2022, **5**(4), 259–267.
13 R. Li, K. Xiang, Z. Peng, Y. Zou and S. Wang, Recent Advances on Electrolysis for Simultaneous Generation of Valuable Chemicals at both Anode and Cathode, *Adv. Energy Mater.*, 2021, **11**(46), 2102292.
14 D. Wang, N. He, L. Xiao, F. Dong, W. Chen, Y. Zhou, *et al.*, Coupling Electrocatalytic Nitric Oxide Oxidation over

Carbon Cloth with Hydrogen Evolution Reaction for Nitrate Synthesis, *Angew. Chem., Int. Ed.*, 2021, **60**(46), 24605–24611.

15 T. Wang, L. Tao, X. Zhu, C. Chen, W. Chen, S. Du, *et al.*, Combined anodic and cathodic hydrogen production from aldehyde oxidation and hydrogen evolution reaction, *Nat. Catal.*, 2021, **5**(1), 66–73.

16 Á. Vass, B. Endrődi and C. Janáky, Coupling electrochemical carbon dioxide conversion with value-added anode processes: An emerging paradigm, *Curr. Opin. Electrochem.*, 2021, **25**, 100621.

17 S. Choi, M. Balamurugan, K. G. Lee, K. H. Cho, S. Park, H. Seo, *et al.*, Mechanistic Investigation of Biomass Oxidation Using Nickel Oxide Nanoparticles in a CO(2)-Saturated Electrolyte for Paired Electrolysis, *J. Phys. Chem. Lett.*, 2020, **11**(8), 2941–2948.

18 J. Bi, Q. Zhu, W. Guo, P. Li, S. Jia, J. Liu, *et al.*, Simultaneous CO2 Reduction and 5-Hydroxymethylfurfural Oxidation to Value-Added Products by Electrocatalysis, *ACS Sustainable Chem. Eng.*, 2022, **10**(24), 8043–8050.

19 J. Woo, B. C. Moon, U. Lee, H.-S. Oh, K. H. Chae, Y. Jun, *et al.*, Collaborative Electrochemical Oxidation of the Alcohol and Aldehyde Groups of 5-Hydroxymethylfurfural by NiOOH and Cu(OH)2 for Superior 2,5-Furandicarboxylic Acid Production, *ACS Catal.*, 2022, **12**(7), 4078–4091.

20 L. Jiang, A. Gonzalez-Diaz, J. Ling-Chin, A. Malik, A. P. Roskilly and A. J. Smallbone, PEF plastic synthesized from industrial carbon dioxide and biowaste, *Nat. Sustainability*, 2020, **3**(9), 761–767.

21 W. Yang, X. Tang, W. Li, X. Luo, C. Zhang and C. Shen, Fast and continuous synthesis of 2,5-furandicarboxylic acid in a micropacked-bed reactor, *Chem. Eng. J.*, 2022, **442**, 136110.

22 S. Li, M. Dong, J. Yang, X. Cheng, X. Shen, S. Liu, *et al.*, Selective hydrogenation of 5-(hydroxymethyl)furfural to 5-methylfurfural over single atomic metals anchored on Nb (2)O(5), *Nat. Commun.*, 2021, **12**(1), 584.

23 P. Zhou, X. Lv, S. Tao, J. Wu, H. Wang, X. Wei, *et al.*, Heterogeneous-Interface-Enhanced Adsorption of Organic and Hydroxyl for Biomass Electrooxidation, *Adv. Mater.*, 2022, **34**(42), e2204089.

24 J. Cui, X. Lu, M. Guo, M. Zhang, L. Sun, J. Xiong, *et al.*, Construction of a g-C3N4-driven photocatalytic system for boosted biomass-derived alcohol oxidation: a promising route towards sustainable biomass valorization, *Catal. Sci. Technol.*, 2023, **13**(4), 940–957.

25 Z. Chen, H. Zhou, F. Kong and M. Wang, Piezocatalytic oxidation of 5-hydroxymethylfurfural to 5-formyl-2-furancarboxylic acid over Pt decorated hydroxyapatite, *Appl. Catal., B*, 2022, **309**, 121281.

26 T. Xia, W. Gong, Y. Chen, M. Duan, J. Ma, X. Cui, *et al.*, Sunlight-Driven Highly Selective Catalytic Oxidation of 5-Hydroxymethylfurfural Towards Tunable Products, *Angew. Chem., Int. Ed.*, 2022, **61**(29), e202204225.

27 Z.-W. Yang, J.-M. Chen, L.-Q. Qiu, W.-J. Xie and L.-N. He, Solar energy-driven electrolysis with molecular catalysts for the reduction of carbon dioxide coupled with the oxidation of 5-hydroxymethylfurfural, *Catal. Sci. Technol.*, 2022, **12**, 5495–5500.

28 S. Choi, M. Balamurugan, K. G. Lee, K. H. Cho, S. Park, H. Seo, *et al.*, Mechanistic Investigation of Biomass Oxidation Using Nickel Oxide Nanoparticles in a CO2-Saturated Electrolyte for Paired Electrolysis, *J. Phys. Chem. Lett.*, 2020, **11**(8), 2941–2948.

29 X. Wei, Y. Li, L. Chen and J. Shi, Formic Acid Electro-Synthesis by Concurrent Cathodic CO2 Reduction and Anodic CH_3 OH Oxidation, *Angew. Chem., Int. Ed.*, 2021, **60**(6), 3148–3155.

30 X. Pang, H. Bai, H. Zhao, W. Fan and W. Shi, Efficient Electrocatalytic Oxidation of 5-Hydroxymethylfurfural Coupled with 4-Nitrophenol Hydrogenation in a Water System, *ACS Catal.*, 2022, **12**(2), 1545–1557.

31 Z.-W. Yang, J.-M. Chen, L.-Q. Qiu, W.-J. Xie and L.-N. He, Solar energy-driven electrolysis with molecular catalysts for the reduction of carbon dioxide coupled with the oxidation of 5-hydroxymethylfurfural, *Catal. Sci. Technol.*, 2022, **12**(18), 5495–5500.

32 O. Simoska, Z. Rhodes, S. Weliwatte, J. R. Cabrera-Pardo, E. M. Gaffney, K. Lim, *et al.*, Advances in Electrochemical Modification Strategies of 5-Hydroxymethylfurfural, *ChemSusChem*, 2021, **14**(7), 1674–1686.

33 Y. Yang and T. Mu, Electrochemical oxidation of biomass derived 5-hydroxymethylfurfural (HMF): pathway, mechanism, catalysts and coupling reactions, *Green Chem.*, 2021, **23**(12), 4228–4254.

34 D. J. Chadderdon, L. Xin, J. Qi, Y. Qiu, P. Krishna, K. L. More, *et al.*, Electrocatalytic oxidation of 5-hydroxymethylfurfural to 2,5-furandicarboxylic acid on supported Au and Pd bimetallic nanoparticles, *Green Chem.*, 2014, **16**(8), 3778–3786.

35 X. Lu, K. H. Wu, B. Zhang, J. Chen, F. Li, B. J. Su, P. Q. Yan, J. M. Chen and W. Qi, Highly Efficient Electro-reforming of 5-Hydroxymethylfurfural on Vertically Oriented Nickel Nanosheet/Carbon Hybrid Catalysts: Structure-Function Relationships, *Angew. Chem., Int. Ed.*, 2021, **133**, 14649–14656.

36 D. Xu, Y. Yang, B. Zhang, Z. Yang, S. Liu and T. Mu, Deep Eutectic Solvent-Induced In Situ Etching and Phosphorization to Form Nickel Phosphides for Electrooxidation of 5-Hydroxymethylfurfural, *ChemSusChem*, 2022, e202200822.

37 D.-H. Nam, B. J. Taitt and K.-S. Choi, Copper-Based Catalytic Anodes To Produce 2,5-Furandicarboxylic Acid, a Biomass-Derived Alternative to Terephthalic Acid, *ACS Catal.*, 2018, **8**(2), 1197–1206.

38 M. Sun, Y. Wang, C. Sun, Y. Qi, J. Cheng, Y. Song, *et al.*, Nitrogen-doped Co3O4 nanowires enable high-efficiency electrochemical oxidation of 5-hydroxymethylfurfural, *Chin. Chem. Lett.*, 2022, **33**(1), 385–389.

39 Y. Sun, J. Wang, Y. Qi, W. Li and C. Wang, Efficient Electrooxidation of 5-Hydroxymethylfurfural Using Co-Doped Ni3 S2 Catalyst: Promising for H2 Production under

Industrial-Level Current Density, *Adv. Sci.*, 2022, **9**(17), e2200957.

40 H. Huang, C. Yu, X. Han, H. Huang, Q. Wei, W. Guo, Z. Wang and J.S. Qiu, Ni, Co hydroxide triggers electrocatalytic production of high-purity benzoic acid over 400 mA cm-2, *Energy Environ. Sci.*, 2020, **13**, 4990–4999.

41 B. You, X. Liu, N. Jiang and Y. Sun, A General Strategy for Decoupled Hydrogen Production from Water Splitting by Integrating Oxidative Biomass Valorization, *J. Am. Chem. Soc.*, 2016, **138**(41), 13639–13646.

42 H. Sheng, A. N. Janes, R. D. Ross, H. Hofstetter, K. Lee, J. R. Schmidt, *et al.*, Linear paired electrochemical valorization of glycerol enabled by the electro-Fenton process using a stable NiSe2 cathode, *Nat. Catal.*, 2022, **5**(8), 716–725.

43 C. Chen, X. Yan, S. Liu, Y. Wu, Q. Wan, X. Sun, Q. Zhu, H. Liu, L. Zheng, H. Wu and B. Han, Highly Efficient Electroreduction of CO2 to C2+ Alcohols on Heterogeneous Dual Active Sites, *Angew. Chem., Int. Ed.*, 2020, **14**, 16601–16606.

44 J. Zhang, Y. Wang, Z. Li, S. Xia, R. Cai, L. Ma, *et al.*, Grain Boundary-Derived Cu(+) /Cu(0) Interfaces in CuO Nanosheets for Low Overpotential Carbon Dioxide Electroreduction to Ethylene, *Adv. Sci.*, 2022, **9**(21), e2200454.

45 H. Li, T. Liu, P. Wei, L. Lin, D. Gao, G. Wang, X. Bao, *et al.*, High-Rate CO2 Electroreduction to C2+ Products over a Copper-Copper Iodide Catalyst, *Angew. Chem., Int. Ed.*, 2021, **133**(26), 14450–14454.

46 Z. Yin, J. Yu, Z. Xie, S.-W. Yu, L. Zhang, T. Akauola, J. Chen, W. Huang, L. Qi, S. Zhang, *et al.*, Hybrid Catalyst Coupling Single-Atom Ni and Nanoscale Cu for Efficient CO2 Electroreduction to Ethylene, *J. Am. Chem. Soc.*, 2022, **144**(45), 20931–20938.

47 H. S. Jeon, J. Timoshenko, C. Rettenmaier, A. Herzog, A. Yoon, S. W. Chee, *et al.*, Selectivity Control of Cu Nanocrystals in a Gas-Fed Flow Cell through CO2 Pulsed Electroreduction, *J. Am. Chem. Soc.*, 2021, **143**(19), 7578–7587.

48 Y. Wang, Z. Wang, C.-T. Dinh, J. Li, A. Ozden and M. G. Kibria, *et.al.,* Catalyst synthesis under CO_2 electroreduction favours faceting and promotes renewable fuels electrosynthesis, *Nat. Catal.*, 2019, **3**(2), 98–106.

49 W. Zhang, C. Huang, Q. Xiao, L. Yu, L. Shuai, P. An, *et al.*, Atypical Oxygen-Bearing Copper Boosts Ethylene Selectivity toward Electrocatalytic CO2 Reduction, *J. Am. Chem. Soc.*, 2020, **142**(26), 11417–11427.

50 Y. Yao, Y. Zhou, X. Liu, Y. Li, D. Wang, X. Chi, *et al.*, Restraining lattice oxygen of Cu2O by enhanced Cu–O hybridization for selective and stable production of ethylene with CO2 electroreduction, *J. Mater. Chem. A*, 2022, **10**(39), 20914–20923.

51 J. Kim, W. Choi, J. W. Park, C. Kim, M. Kim and H. Song, Branched Copper Oxide Nanoparticles Induce Highly Selective Ethylene Production by Electrochemical Carbon Dioxide Reduction, *J. Am. Chem. Soc.*, 2019, **141**(17), 6986–6994.